Phase Transitions, 2013
Vol. 86, No. 1, 67–87, http://dx.doi.org/10.1080/01411594.2012.695373

Taylor & Francis
Taylor & Francis Group

Ferrimagnetic/ferroelastic domain interactions in magnetite below the Verwey transition. Part I: electron holography and Lorentz microscopy

Takeshi Kasama[a]*, Richard J. Harrison[b], Nathan S. Church[b], Masahiro Nagao[c], Joshua M. Feinberg[d] and Rafal E. Dunin-Borkowski[ae]

[a]*Center for Electron Nanoscopy, Technical University of Denmark, DK-2800 Kongens Lyngby, Denmark;* [b]*Department of Earth Sciences, University of Cambridge, Downing Street, Cambridge CB2 3EQ, UK;* [c]*Advanced Materials Laboratory, National Institute for Materials Science, 1-1 Namiki, Tsukuba, Ibaraki 305-0044, Japan;* [d]*Institute for Rock Magnetism, Department of Geology and Geophysics, University of Minnesota, Minneapolis, MN 55455, USA;* [e]*Ernst Ruska-Centre for Microscopy and Spectroscopy with Electrons and Peter Grünberg Institute, Research Centre Jülich, D-52425 Jülich, Germany*

(*Final version received 16 May 2012*)

The crystallographic and magnetic microstructure of magnetite (Fe_3O_4) below the Verwey transition (~120 K) is studied using transmission electron microscopy. The low temperature phase is found to have a monoclinic *C*-centered lattice with a *c*-glide plane perpendicular to the *b*-axis, which allows twin-related crystal orientations to be distinguished. Off-axis electron holography and Lorentz electron microscopy are used to show that magnetic domains present at room temperature become subdivided into sub-micron-sized magnetic domains below the Verwey transition, with the magnetization direction in each magnetic domain oriented along the monoclinic [001] axis. The nature of the interactions between the magnetic domain walls and the ferroelastic twin walls is investigated. Cooling and warming cycles through the transition temperature are used to show that a memory effect is likely to exist between the magnetic states that form above and below the transition. Our results suggest that ferroelastic twin walls have a strong influence on the low temperature magnetic properties of magnetite.

Keywords: magnetite; Verwey transition; low temperature magnetic properties; ferroelastic twins; multiferroics; transmission electron microscopy

1. Introduction

The Verwey transition has a profound impact on the physical and magnetic properties of magnetite (Fe_3O_4) [1–3]. Below a transition temperature of ~125 K, magnetite transforms from a cubic to a monoclinic [4–13] structure, resulting in an order of magnitude increase in magnetocrystalline anisotropy [14,15]. The combination of enhanced anisotropy with the pervasive development of fine-scale ferroelastic twinning has dramatic consequences for the ferromagnetic domain structure, due to the enforced switching of magnetocrystalline easy axes that occurs across twin domain boundaries [16–28]. Understanding the nature of the interaction between magnetic domain boundaries and ferroelastic twin

*Corresponding author. Email: tk@cen.dtu.dk

© 2013 Taylor & Francis

boundaries is of critical importance, not only in magnetite, but also in multiferroic materials in general. In Part I of this article we use several TEM techniques including electron diffraction, Lorentz imaging and off-axis electron holography to examine the nature of the interactions between ferroelastic twins and ferrimagnetic domain walls below the Verwey transition in magnetite. In Part II, we demonstrate how these experimental observations can be explained theoretically using micromagnetic simulations, and develop an image simulation methodology that allows direct comparison between experiment and theory.

Kasama et al. [29] carried out the first TEM measurements to image both the magnetic and the crystallographic microstructure of magnetite below the Verwey transition. They identified three distinct types of ferroelastic twin boundaries, each of which has a fundamentally different impact on the orientation of the magnetocrystalline anisotropy axes. Here we provide new crystallographic and magnetic information about each of these twin boundary types, and describe *in situ* microscopic observations of how magnetic information is transferred between the cubic and monoclinic phases on cooling and warming through the Verwey transition. These observations are of particular relevance to rock magnetic studies, where cooling and warming through the Verwey transition in zero-field conditions is commonly used as a method to demagnetize multi-domain magnetite particles prior to subsequent paleomagnetic analysis.

2. Experimental details

Polycrystalline magnetite was synthesized by pressing a pellet of Fe_2O_3 powder, firing it for 24 h at 1573 K in an oxygen fugacity $f_{O_2} = -5.3$ (99.4% CO_2; 0.6% CO) and then quenching it into water. The resulting grain size was typically 10–30 μm. Magnetic susceptibility measurements showed a clear Verwey transition at 120 K. Measurements of saturation magnetization ($87\,Am^2\,kg^{-1}$), coercivity (0.72 mT) and Curie temperature (853 K) confirmed it to be multi-domain magnetite with the composition of its end-member. For TEM examination, the sample was polished mechanically down to 20-μm-thick slices, which were then thinned to electron transparency by Ar ion milling.

A Philips CM300 field emission gun (FEG) TEM and an FEI Titan 80-300ST FEG TEM, both equipped with a Lorentz minilens and an electrostatic biprism, were used to study the sample in magnetic-field-free conditions at an accelerating voltage of 300 kV. Electron diffraction experiments were carried out on these microscopes, as well as on an FEI Tecnai T20 TEM operated at 120 kV and on a Hitachi HF3000L TEM operated at 300 kV. The HF3000L allows lateral magnetic fields of up to ~60 mT to be applied to specimens *in situ* in the TEM.

The Fresnel mode of Lorentz electron microscopy and off-axis electron holography were used to study magnetic properties of the magnetite specimen both above and below the Verwey transition. Lorentz electron microscopy allows changes in magnetic microstructure to be recorded dynamically either in the absence or in the presence of an applied magnetic field. The image contrast results from deflection of the incident electron beam by the Lorentz force associated with the in-plane component of the magnetization in the specimen and gives rise to bands of bright or dark intensity at the positions of magnetic domain walls, from which the direction of the local magnetic moment in the specimen can often be inferred [30].

Off-axis electron holography has been used to characterize the magnetic microstructure of a wide variety of materials with high spatial resolution [31–35]. The technique involves

using an electrostatic biprism to overlap the electron wave that passes through the region of interest on the sample with another part of the electron wave that passes only through vacuum to form a holographic interference fringe pattern that contains information about both the amplitude and the phase shift of the electron wave that passes through the sample [36]. The phase shift can be used to quantify the in-plane component of the magnetic induction within and around the specimen integrated in the electron beam direction. In general, the desired magnetic phase shift must be separated from the mean inner potential (MIP) contribution to the phase shift using approaches that are described elsewhere [36]. In this study, however, our experimental observations revealed that there was no significant difference between magnetic induction maps obtained with and without the elimination of the MIP contribution. For this reason, the magnetic induction maps presented in this article contain the MIP contribution in order to avoid introducing additional artifacts during image processing. This approach proved to be reliable both because the present sample was a single-phase material and because the sample was relatively uniform in thickness.

Selected-area electron diffraction (SAED) and convergent-beam electron diffraction (CBED) were used to determine the space group and crystallographic orientation of each region of interest and to identify local twin variants through comparisons with diffraction patterns simulated using 'JEMS' electron microscopy simulation software [37]. For the simulations we used a structural model proposed by Zuo et al. [7], with monoclinic *Cc* symmetry with $a = 1.1868\,\text{nm}$, $b = 1.1851\,\text{nm}$, $c = 1.6752\,\text{nm}$, and $\beta = 90.2^\circ$, since our examination for the space group confirmed that low temperature magnetite had monoclinic *Cc* symmetry (see 'Confirmation of space group *Cc*').

The relationship between the low temperature monoclinic (m) cell and the high temperature cubic (c) cell is given in Figure 1. The change in point group symmetry from *m3m* to *m* on decreasing the temperature below the Verwey transition results in 24 possible crystallographic orientations of the monoclinic phase with respect to the cubic phase [29]. Although the $[001]_m$ axis can lie along any $\langle 001\rangle_c$ direction of the parent cubic phase, by

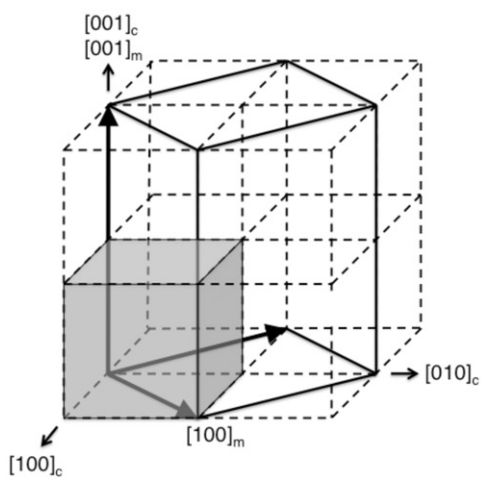

Figure 1. Relationship between crystallographic axes in magnetite in the monoclinic unit cell below the Verwey transition (solid line) and the cubic unit cell above the Verwey transition (shown in grey). The monoclinic distortion ($\beta = 90.2^\circ$) is not shown.

convention we set $[001]_m//[001]_c$, $[100]_m//[110]_c$ and $[010]_m//[\bar{1}10]_c$. The spontaneous strain tensor corresponds to a rhombohedral distortion of the pseudo-cubic unit cell, with the axis of elongation parallel to $[111]_c$. In the cubic phase, the magnetic easy axes are $\langle 111\rangle_c$ for $T > 130\,\mathrm{K}$ and $\langle 100\rangle_c$ for $120 < T < 130\,\mathrm{K}$, where the first cubic-magnetocrystalline anisotropy constant is zero [15]. In the monoclinic phase, the easy, intermediate and hard axes are $[001]_m$, $[010]_m$ and $[100]_m$, respectively.

3. Results and discussion

Figure 2 shows conventional TEM images and corresponding SAED patterns recorded from synthetic magnetite above and below the Verwey transition, which was observed to take place at 120 K. Below the transition, twin domains with widths of between ~20 nm and 5 μm form as a result of the transformation from the cubic to the monoclinic phase. The SAED patterns below the transition show additional low order reflections, whose intensities are ~1000 times lower than those of the strong fundamental reflections (Figure 2d).

3.1. *Confirmation of space group Cc*

Previous CBED work [4] for the low temperature phase of magnetite revealed the presence of a *c*-glide plane, which was determined from dynamical extinction lines for

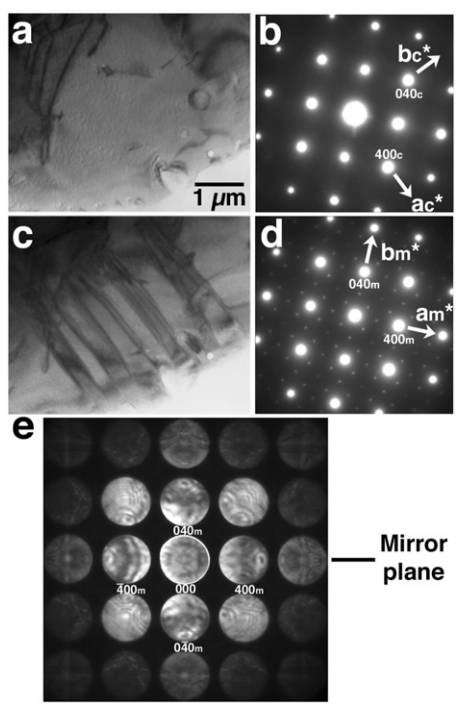

Figure 2. Conventional TEM images and corresponding SAED patterns recorded from the same region of a synthetic magnetite specimen; (a, b) above and (c, d) below the Verwey transition. In (c), *ab*-twining about the monoclinic *c*-axis is observed, with the monoclinic *a*- and *b*-axes interchanged between adjacent twins. Line-like contrast in (a) and (c) originates from dislocations. (e) Energy-filtered convergent-beam electron diffraction pattern acquired from $[001]_m$ magnetite below the Verwey transition, showing only strong fundamental reflections.

$00l$ ($l = 2n+1$) and 2, 0, ±43 reflections, as well as a mirror plane in an $[001]_m$ CBED pattern, providing evidence that the space group is *Cc*. Zuo et al. [7] also noted the absence of ±20, 0, 1 reflections, which should not be present kinematically if the crystal has a *c*-glide plane. The determination of the space group is complicated by the fact that the vertical magnetic field of the microscope objective lens forces the magnetic easy axis $[001]_m$ into the direction parallel to the electron beam, making it difficult to obtain diffraction patterns with the monoclinic *c*-axis perpendicular to the electron beam direction. Therefore, the sample was cooled below the Verwey transition in zero field to increase the proportion of domains with an in-plane monoclinic *c*-axis. SAED patterns were acquired in conventional TEM mode with the objective lens switched on.

Figure 3 shows experimental SAED patterns acquired from magnetite at various zone axis orientations at 90–100 K, whose temperature is well below the Verwey transition. In the $[001]_m$ pattern shown in Figure 3(b), reflections for which $h+k = 2n+1$ are absent, indicating that the lattice type is *C*-centered. In the $[1\bar{1}0]_m$ pattern, $00l$ ($l = 2n+1$) reflections, which are forbidden due to the presence of a *c*-glide plane, are absent or very weak (Figure 3a). The fact that $00l$ ($l = 2n+1$) and $h0l$ (h, $l = 2n+1$) reflections are absent in the $[010]_m$ pattern shown in Figure 3(e) is also consistent with the presence of a *c*-glide plane. Note that the forbidden reflections for the presence of a *c*-glide plane often exist in diffraction patterns due to dynamical multiple scattering (e.g., $00l$ ($l = 2n+1$) reflections in the $[100]_m$ pattern). The $[001]_m$ CBED pattern appears to have a mirror plane perpendicular to $[010]_m$ and does not show higher symmetry (such as $2mm$ for point group $2/m$ in the projected pattern), suggesting that the point group is *m* (Figure 2e).

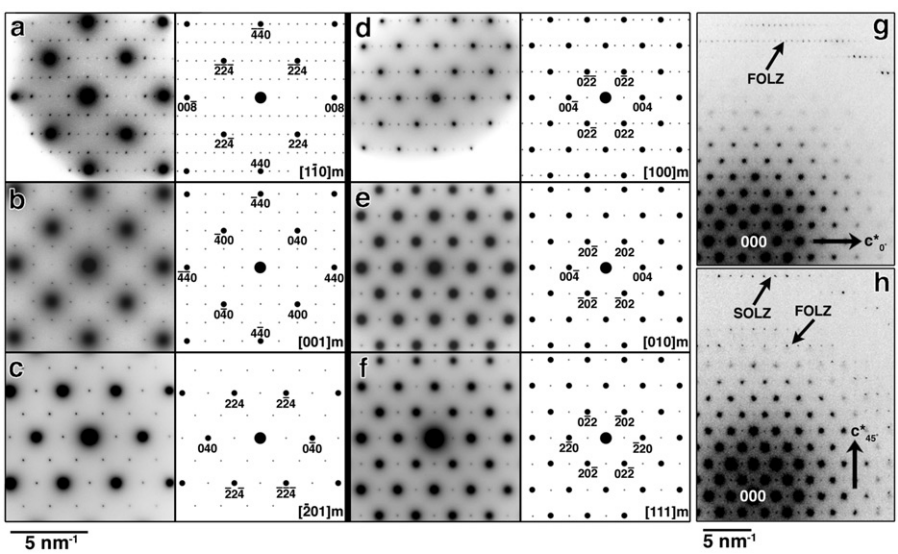

Figure 3. (a–f) Experimental SAED patterns recorded from several orientations of magnetite below the Verwey transition and corresponding kinematic simulations assuming space group *Cc*. In the experimental pattern in (d), the $00l$ reflections ($l = 2n+1$) are due to dynamical multiple scattering. (g, h) Experimental SAED patterns acquired from $[010]_m$ and $[111]_m$ magnetite below the Verwey transition, showing different reflections in the higher-order Laue zones (arrowed). The symbols '$c^*_{0^\circ}$' and '$c^*_{45^\circ}$' refer to monoclinic *c*-axes that are oriented in the plane and at 45° to the plane of the specimen, respectively.

From these measurements, therefore, the space group of low temperature magnetite was found to be *Cc*, in agreement with previous studies [4–7].

3.2. *Determination of crystallographic orientation*

Kinematic simulations of SAED patterns were carried out for space group *Cc* using the lattice parameter proposed by Zuo et al. [7] for comparison with the experimental SAED patterns shown in Figure 3(a–f). Dynamical diffraction patterns were also calculated using the crystal structure model of Zuo et al. [7] (not shown). Although there are some differences in the dynamical diffraction intensity, the similarity of the experimental and kinematically calculated patterns suggest that space group *Cc* is an adequate model for interpreting the low-temperature diffraction patterns of magnetite.

Figure 3 confirms that magnetite has different monoclinic $[001]_m$ and $[1\bar{1}0]_m$ or $[110]_m$ diffraction patterns, whereas the equivalent patterns for the cubic phase are identical. The $[1\bar{1}0]_m$ and $[110]_m$ patterns show closer-spaced reflections with a *d*-spacing of 1.6 nm along the monoclinic *c*-axis, due to *c*-axis doubling (Figure 3a). The $[1\bar{1}0]_m$ and $[110]_m$ patterns cannot be distinguished from each other within the accuracy of the current diffraction experiment. In the $[001]_m$ pattern, the monoclinic *a*- and *b*-axes are distinguishable by the absence or low intensity of $h0l$ ($l = 2n + 1$) reflections in the first-order Laue zone (FOLZ) and by the greater intensity of the 020 reflection in comparison to the 200 reflection. The latter relationship is predicted to be independent of specimen thickness according to dynamical calculations.

In the cubic $\langle 110\rangle_c$ orientations, there are three different diffraction patterns present in the low-temperature phase: $[100]_m$, $[010]_m$ and $[111]_m$. The $[100]_m$ pattern has distinctive reflections in the zeroth-order Laue zone (ZOLZ) as a result of *c*-axis doubling (Figure 3d). The patterns for $[010]_m$ and $[111]_m$ (Figure 3e and f) are almost the same in the ZOLZ but have characteristic features in the higher-order Laue zone (HOLZ). The $[010]_m$ pattern has closely spaced reflections that are related to the monoclinic *c*-axis in the first-order Laue zone (FOLZ), whereas they are absent for $[111]_m$. This difference allows each orientation to be distinguished unambiguously. When viewed from directions that are equivalent to $[111]_m$ (e.g., $[1\bar{1}1]_m$ or $[\bar{1}1\bar{1}]_m$), the patterns are identical to each other and cannot be distinguished within the accuracy of this diffraction experiment (Figure 3f).

As there are no significant differences between the diffraction patterns for the orientations that were originally cubic $\langle 111\rangle_c$, their crystallographic orientations cannot be distinguished at low temperature (Figure 3c). Despite these limitations, the crystallographic orientations of individual magnetite twin domains can be determined sufficiently well for the purpose of the present study.

3.3. *Propagation of monoclinic domains*

As expected for a first-order phase transition, co-existence of the high and low temperature phases is observed as the transition proceeds. Figure 4 shows a video frame sequence, illustrating how the cubic phase is gradually replaced by the growing monoclinic phase during zero field cooling (see Supplementary Movie 1 in Kasama et al. [29]). Above the transition temperature, no twins are present in the cubic phase (Figure 4a). The band-like contrast results from dynamical diffraction, associated with local changes in specimen shape, thickness and/or strain. With decreasing temperature, the monoclinic phase develops from the top and bottom (Figure 4b and c). The boundaries between the cubic

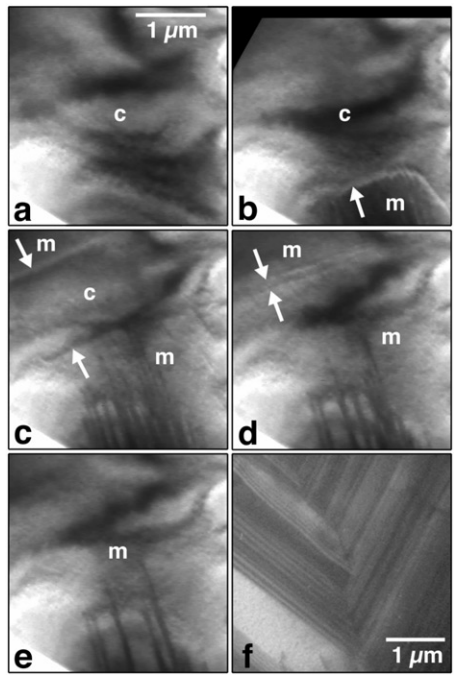

Figure 4. (a–e) Time sequence of conventional TEM images showing the development of monoclinic magnetite domains across the Verwey transition, captured using a video recorder. The viewing direction is $[111]_c$. The specimen cooling rate is approximately 0.08°C/s. The relative time at which each image was recorded is: (a) 0, (b) 12, (c) 21, (d) 33 and (e) 54 s. The arrows show the positions of phase boundaries, with 'c' and 'm' referring to cubic and monoclinic regions, respectively. (f) Type 1 twin boundary in monoclinic magnetite across which the *c*-axes of neighboring domains change by 90°. The *c*-axis in each domain is oriented perpendicular to the fine-scale Type 2 twins.

and monoclinic phases (indicated by the white arrows) are straight and sharp, and sweep through the crystal at a speed of ~100 nm/s when the temperature is decreased by 0.08°C/s. In Figures 4(a–e), the upper and lower monoclinic domains happen to have the same monoclinic *c*-axis orientation (the projected monoclinic *c*-axis is perpendicular to fine-scale Type 2 twin planes present in the bottom domain – see Section 3.4 for a definition of twin types) and a single larger domain is formed on impingement. In contrast, when neighboring domains with different monoclinic *c*-axis orientations impinge, they form an irregular domain boundary, as shown in Figure 4(f). The monoclinic domains on each side of this boundary are subdivided by fine-scale lamellar and/or needle twins. These fine-scale twins lie perpendicular to the monoclinic *c*-axis, which changes its orientation by ~90° on crossing the irregular boundary. The needle twins remain mobile below the transition temperature via a mechanism of advancement or retraction of their needle tips (a mechanism that dominates twin dynamics in ferroelastic materials under conditions of low applied stress [38–40]). Needle tip displacement occurs in response to stresses that develop as a consequence of thermal contraction during continued cooling, or through local heating by the electron beam [41].

Our observations show that the monoclinic phase is able to develop from the specimen edge, as shown in Figure 4, while Otsuka and Sato [27] found only the cubic phase close to the specimen edge and only the monoclinic phase in thicker regions away from the

specimen edge. The difference between these observations can be explained by local heating of the specimen by the electron beam. When we used a TEM equipped with a LaB_6 gun, which produces an electron beam current much larger than that of the FEG TEM used in this study, a similar phenomenon to that seen by Otuska and Sato [27] was observed, i.e., thinner regions close to the specimen edge were heated above the transition temperature.

3.4. *Types of ferroelastic twin*

Three primary types of ferroelastic twin are observed in magnetite at low temperature [29]. Type 1 twins involve a 90° change in the monoclinic *c*-axis direction, and hence a 90° switch in the magnetocrystalline easy axis (Figure 4f). Type 1 twin boundaries are typically irregular and are readily identified in conventional TEM images by the sudden change in orientation of the finer scale twins (Type 2) across the boundary. Type 1 twins are formed when monoclinic domains with different crystallographic orientations, which nucleated independently at different sites, merge together, as shown in Figure 4(f). Occasionally, Type 1 twin boundaries do not produce any strain contrast in conventional TEM images, as the orientation of the spontaneous strain tensor is identical in adjacent domains [29]. Such 'invisible' Type 1 twins are referred to as Type 1′, but are otherwise identical to Type 1 twins. Type 2 twins are related by reflection in the $(001)_m$ plane and exist mostly as fine-scale twins within large monoclinic domains. This operation creates a change in the orientation of the spontaneous strain, but leaves the magnetic easy, intermediate and hard axes unchanged [29]. Type 3 twins are related to each other by a 90° rotation about the monoclinic *c*-axis, such that the magnetic easy axis is left unchanged but the intermediate *b*-axis and hard *a*-axis are interchanged (Figure 2c and d). Although some studies have reported the presence of zigzag monoclinic *c*-axis twinning in which neighboring domains share their monoclinic *a*- and *b*-axes [7,13,26], such relationships were not observed in this study, perhaps because of a lack of visibility when the viewing orientations are close to $[001]_m$ and/or because of a lack of sensitivity in the detection of split twin reflections.

3.5. *Magnetic structure above the Verwey transition*

Lorentz images recorded at room temperature show magnetic domains with sizes in the range of 500 to 3000 nm, which are usually separated by 180° magnetic domain walls. 90° magnetic domain walls and vortex states are observed locally in regions close to the specimen edge (Figures 5a and 6b and c).

Unlike Lorentz imaging, off-axis electron holography provides quantitative magnetic information, although it suffers from the drawback that only regions close to the specimen edge can be examined. Figure 6(b) and (c) show remanent magnetic states recorded at room temperature from the region marked '1' in Figure 5(a), after applying magnetic fields in different directions. Figures 5(a) and 6(c) correspond to the same magnetic state.

These magnetic states are usually reproducible after the same field is applied and their details depend on the applied field direction. This behavior results from the absence of crystallographic defects, which would act as pinning sites. The magnetization direction changes gradually and follows the specimen edge in most cases. 90° magnetic domain walls, which are visible in Figure 6(b), are present primarily in the form of closure domains at the specimen edge [42]. In Figure 6(c), the vortex states shown in Figure 5(a) as bright

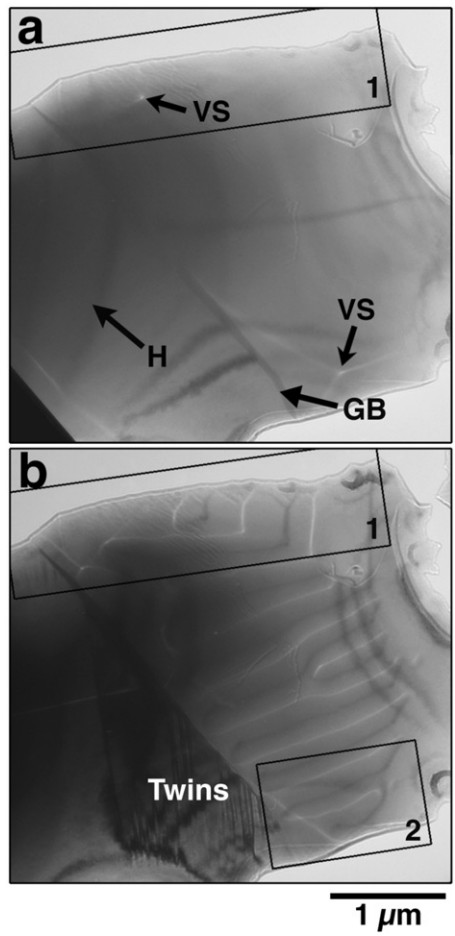

Figure 5. Lorentz images acquired from the same region of a magnetite specimen (a) above and (b) below the Verwey transition. The arrow marked 'H' indicates the applied magnetic field direction. The image in (b) was obtained at remanence after the sample was cooled from the magnetic state shown in (a) to 120 K in zero field. Boxes '1' and '2' indicate regions examined using off-axis electron holography in Figures 6 and 7, respectively. The images were acquired at an overfocus of 317 μm. GB: grain boundary, VS: vortex state.

spots are clearly observed, although the direction and magnitude of the magnetization are affected by the local thickness variation of the specimen.

3.6. *Magnetic structure below the Verwey transition*

Below the Verwey transition, the magnetic structure is significantly different from that observed at room temperature, with a stripe-like magnetic remanent state visible in Figure 5(b). The magnetic domain structure is more complicated, with domain sizes that can be as small as several tens of nanometres. Similar complexity has been observed on a different length scale by magnetic force microscopy (MFM) [28].

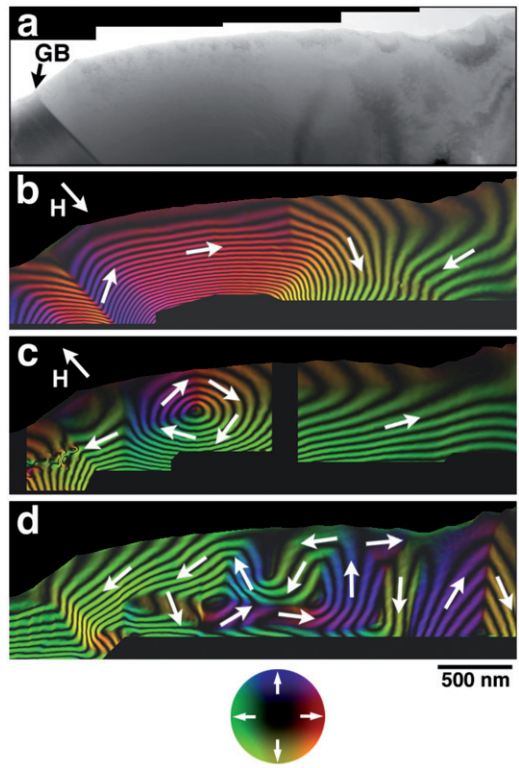

Figure 6. (a) Conventional TEM image and (b–d) magnetic induction maps (1 × phase amplification) recorded using electron holography from the region marked '1' in Figure 5. The images in (b) and (c) were acquired at room temperature at remanence after applying a 1 T in-plane field to the specimen in opposite directions and reducing this field to zero. The arrows marked 'H' indicate the applied magnetic field directions. The irregular feature visible on the left side of (c) is an artifact caused by diffraction contrast. The image in (d) was acquired at remanence after the magnetic state shown in (c) was cooled to below 120 K in zero field. The white arrows on the induction maps show the local magnetization directions. The direction of the magnetic induction is also shown according to a color wheel (red = right, yellow = down, green = left, blue = up). GB: grain boundary.

Figure 6(d) shows a magnetic induction map measured using electron holography from the region marked '1' in Figure 5(b), showing closure domains at the specimen edge. Previous micromagnetic simulations for pseudo-single domain magnetite crystals predicted that closure domains are unfavorable in monoclinic magnetite [43], while MFM observations also indicated the absence of closure domains in low temperature magnetite [28]. In Part II, Bryson et al. [44] investigate the possibility that closure domains are able to form by the presence of Type 1 twins by means of micromagnetic simulations. They suggest that the closure domains present in the monoclinic phase of magnetite can be caused by the formation of ferroelastic twin domains, whose *c*-axes are at ~90° to each other. The magnetic domains that are further from the specimen edge have widths of 100–500 nm and are separated by 180° domain walls as a result of the large uniaxial magnetocrystalline anisotropy of the monoclinic phase.

Kasama et al. [29] reported three characteristic magnetic states in magnetite below the Verwey transition using TEM and micromagnetic simulations. Here, we present additional observations of their magnetic states and a newly described magnetic state.

In most cases, the magnetization direction in each ferroelastic domain is found to be parallel to the $[001]_m$ easy axis. The most important magnetic structure is associated with the formation of immobile 90° magnetic domain walls, resulting from a change of the $[001]_m$ easy axis to an alternative $\langle 001\rangle_c$ direction (the angle between the monoclinic *c*-axes of the neighboring domains is then 90°). 90° magnetic domain walls are observed both at Type 1 and Type 1′ twin boundaries, where two monoclinic domains merge (e.g., Figure 4f). In addition, Type 1′ boundaries can form much finer scale stripe-like magnetic features within a given region (Figure 5b). The 90° domain walls are immobile in the sense that they can only exist at the twin boundaries and always appear at the same position at remanence even after the application of a 2 T field. This observation implies that Type 1 and Type 1′ twin walls themselves do not move in response to an applied magnetic field at temperatures well below the transition temperature. Video evidence suggests, however, that Type 1 and Type 1′ twin boundaries do become mobile at temperatures approaching the transition temperature and may then be influenced by the application of a magnetic field [29].

The stripe-like Lorentz contrast as shown in Figure 5(b) can result from the presence of a series of immobile 90° domain walls, which are associated with Type 1′ or "strain-contrast-free" twins [29]. Although one might intuitively interpret such stripe-like contrast in a Lorentz image as originating from free-standing 180° Bloch walls, electron holography clearly shows that the contrast results from a zigzag magnetic configuration (Figure 7). The magnetization direction follows the $[001]_m$ easy axis of each twin domain and changes by close to 90° at each twin boundary. The magnetic domain walls appear at the same positions even after applying large fields in opposite directions, indicating that they are defined strictly by underlying crystallographic features. Figure 7(b) shows an electron holographic magnetic induction map simulated using the approach of Beleggia and Zhu [45], superimposed on the experimental Lorentz image. The parameters used are given in the figure caption. The monoclinic *c*-axis direction in each domain was determined from a SAED pattern, which indicated that the neighboring monoclinic *c*-axes are at 90° to each other. The variation in specimen thickness was also considered in the simulation in the form of a wedge, which was measured experimentally from a t/λ map obtained by using electron energy-loss spectroscopy (λ is the inelastic mean free path of electrons in the sample and is estimated to be ~170 nm for magnetite at an accelerating voltage of 300 kV [31] and t is the specimen thickness). Despite the fact that the parameters used in the simulation were slightly different from the true specimen geometry, the agreement with the experimental result is satisfactory, except for the magnetization direction in the purple domains. This inconsistency may be caused by stray magnetic fields associated with the fact that the $[001]_m$ easy axis direction in one of the twin domains points ~45° out of the specimen plane. Micromagnetic simulations suggest that the observed zigzag magnetic structure cannot exist without the presence of twins [44]. Thus, these observations and simulations apparently suggest that the magnetic structure is associated with the presence of ferroelastic twin domains.

The second important magnetic feature in the monoclinic phase is the presence of mobile 180° magnetic domain walls, which normally intersect fine-scale Type 2 twins at ~90° and separate magnetic domains that are magnetized parallel and antiparallel to the $[001]_m$ easy axis (Figure 8a). Lateral motion of these domain walls is observed in applied fields as low as 1–2 mT, but is impeded by pinning at fine-scale needle tips [29]. Type 2 twins are associated with a change in the orientation of the spontaneous strain, but not with a change in the orientation of the magnetic easy, intermediate or hard axes.

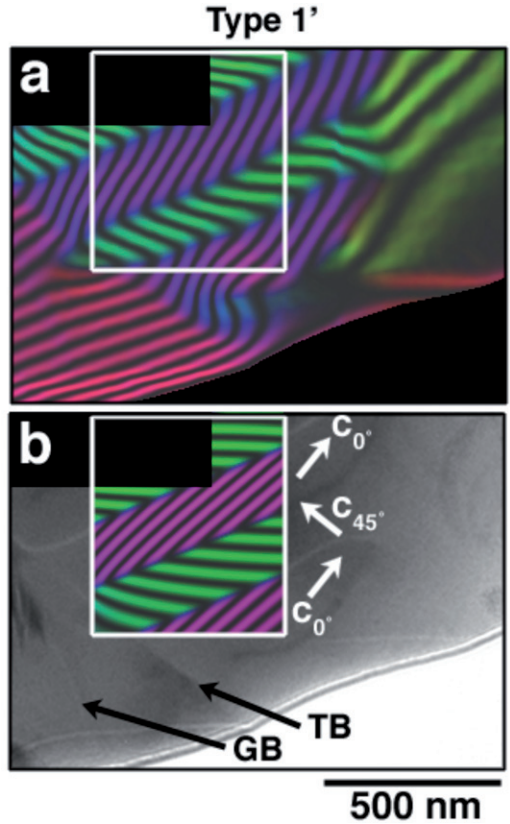

Figure 7. (a) Experimental magnetic induction map (1 × phase amplification) showing Type 1′ twins recorded using electron holography at remanence from the region marked '2' in Figure 5(b) after zero field cooling. (b) Simulated electron holographic induction map overlaid onto the experimental Lorentz image acquired at an overfocus of 317 μm. The parameters used in the simulation were: 0.6 T for the magnetic induction, 17 V for the MIP, 165 nm for the width of each twin domain. The wedge-shaped specimen thickness increases by a gradient of 10% from the 110-nm-thick specimen edge. The symbols '$c_{0°}$' and '$c_{45°}$' refer to *c*-axes that are oriented in-plane and at 45° to the plane of the specimen, respectively. GB: grain boundary, TB: monoclinic twin boundary.

Hence, mobile 180° domain walls show no deflection on crossing Type 2 twin boundaries (Figure 8a).

The third magnetic feature is fine-scale zigzag magnetic domains (Figure 8b), which are associated with Type 3 twins that have a common $[001]_m$ easy axis but an interchanged intermediate monoclinic *b*-axis and hard monoclinic *a*-axis. Such zigzag magnetic features are observed only when the $[001]_m$ axis is oriented significantly out of the specimen plane, as the demagnetizing field of the thin TEM foil then causes the magnetization direction to rotate towards the intermediate *b*-axis. This suggests that this magnetic feature may only be of importance in thinned TEM specimens.

A fourth type of magnetic structure (Figure 8c) results in similar Lorentz contrast to that shown by the Type 1′ magnetic state in Figure 5(b). However, it is associated with the presence of 180° magnetic domain walls, as seen in uniaxial magnetic materials such as *hcp* cobalt [46]. The domain sizes, which are typically a few hundred nanometers, are even smaller than those of 180° lamellar domains that are observed in the cubic phase [42].

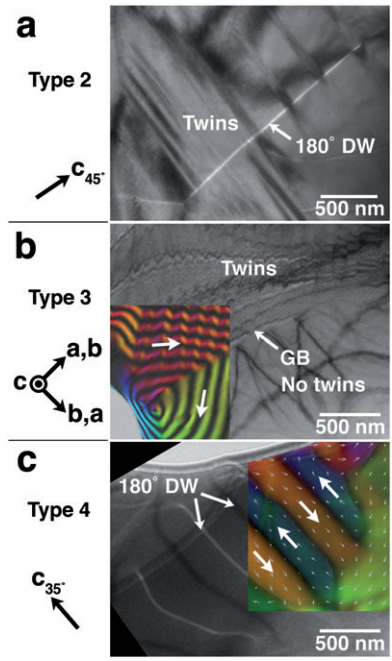

Figure 8. Lorentz images recorded below the Verwey transition, showing (a) Type 2, (b) Type 3 and (c) Type 4 twins. The symbols 'c_{35°' and 'c_{45°' refer to *c*-axes that are oriented at 35° and at 45° to the plane of the specimen, respectively. Magnetic induction maps measured using electron holography are overlaid onto (b) and (c). Phase contours (1 × phase amplification) are shown on (b), while thin arrows have been added to the induction map in (c). Local magnetization directions are also shown with white arrows on the induction maps. The Lorentz images were acquired at an overfocus of 317 μm. GB: grain boundary, DW: magnetic domain wall.

This magnetic state of Type 4 can form in large monoclinic domains that do not contain ferroelastic twins and is thought to develop to reduce the magnetostatic energy. The domain walls are not pinned at crystallographic features and appear at different positions depending on the applied magnetic field.

3.7. Magnetic-field-dependent crystallographic orientations

It is widely accepted that the application of an external magnetic field during cooling affects the choice of monoclinic *c*-axis (e.g., [47]). Figure 9 shows the effect on twin formation of an external magnetic field on cooling through the Verwey transition. In this area, the viewing direction is $[110]_c$ and one of the principal cubic axes (i.e., $[001]_c$) lies almost in the specimen plane (~5° off). When the sample was cooled in zero field, the monoclinic *c*-axis formed primarily in the specimen plane (Figure 9a and b). Since the magnetization in the cubic phase is mostly in-plane, it is perhaps to be expected that this will dictate the orientation of the monoclinic *c*-axis during the transformation.

Figure 9(c) and (e) show the effect on twin formation of the application of an external field to the sample during cooling. In Figure 9(c), a 2T field was applied in the $[111]_c$ direction, which should result in an equal probability for any one of the three cubic axes to become the monoclinic *c*-axis. However, as the sample was tilted by 35° from the cubic

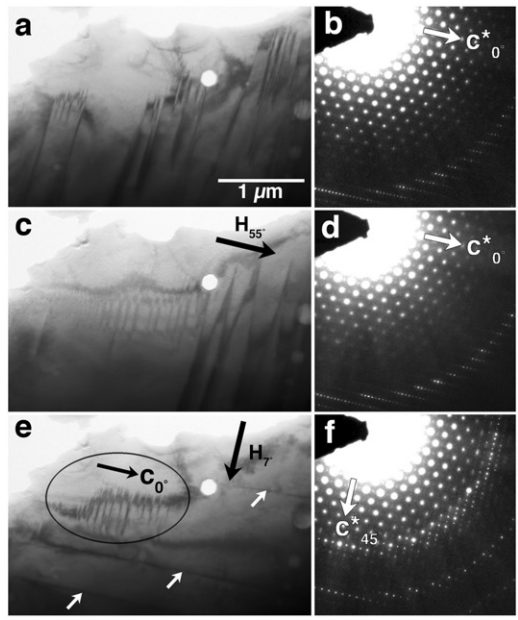

Figure 9. Conventional TEM images and corresponding SAED patterns recorded from a magnetite $[110]_c$ orientation, after cooling the specimen to below the Verwey transition under different conditions: (a, b) zero-field cooling; (c–f) cooling in a field of 2 T applied along a direction close to one of the principal cubic axes. The arrows marked 'H' show the components of the applied field in the plane of the specimen, with the subscripts indicating the angles to the closest principal axes. In (e), the white arrows indicate twin domain boundaries. In the region marked with a black ellipse the monoclinic *c*-axis is in the plane of the specimen, while other regions have their *c*-axis oriented partially out of the plane of the specimen. In the diffraction patterns, the symbols '$c^*_{0^\circ}$' and '$c^*_{45^\circ}$' refer to monoclinic *c*-axes that are oriented in-plane and at 45° to the plane of the specimen, respectively.

$(110)_c$ plane about the $[\bar{1}10]_c$ axis, the sample was subjected to a significant in-plane (~1 T) component of the applied field in the direction parallel to the cubic axis that lay in the plane of the sample. As a result, the in-plane cubic axis became the monoclinic *c*-axis. Twins were observed even after cooling in a large field, with an appearance similar to that of twins formed after zero field cooling. The twin types in Figure 9(a) and (c) were not identified because of the absence of split twin reflections in the SAED patterns (Figure 9b and d). In contrast, when a magnetic field was applied in a direction (~7° off) close to a cubic principal axis (i.e., $[100]_c$) that was oriented at an angle of 45° from the $(110)_c$ plane, the monoclinic *c*-axis formed in the direction of the field (Figure 9e and f). These observations suggest that both internal and external magnetic fields can control the direction of the monoclinic *c*-axis. This behavior was also seen during observations using an HF-3000L TEM, in which the application of lateral magnetic fields to the sample increased the proportion of domains with a monoclinic in-plane *c*-axis.

Unexpectedly, a monoclinic domain with an in-plane *c*-axis were observed close to the specimen edge, in the region marked with a circle in Figure 9(e), even though a large magnetic field was applied perpendicular to the monoclinic in-plane *c*-axis. The formation of the monoclinic domains is likely to be related to the specimen thickness and/or shape since they are only present at the specimen edge. Such crystallographic domains that have

a monoclinic *c*-axis parallel to the specimen edge could be associated with the origin of closure domains that appear often at the specimen edge to reduce the magnetostatic demagnetizing field energy since the monoclinic domains are formed when a significant magnetization orients toward the specimen edge (Figures 5b, 6d and 10). The observation is consistent with results of micromagnetic simulations [44].

Although it is commonly assumed that the application of a large field during cooling prevents twin formation and transforms the cubic axis closest to the applied magnetic field into the monoclinic *c*-axis (e.g., [20]), our results show that the process of twin formation is complicated and that the monoclinic *c*-axis can adopt a direction perpendicular to the applied field. We note, however, that this behavior may be specific to thin TEM samples, and may not be representative of bulk magnetite.

3.8. Low temperature magnetic memory

In order to investigate the evolution of magnetic domains during zero field cooling and warming cycles across the Verwey transition, the following experiments were carried out: (1) a Lorentz image was initially acquired at 143 K (above the Verwey transition) after applying a 2 T field to the sample tilted at $+30^\circ$ at $\sim$150 K; (2) a second image was obtained at 103 K (below the Verwey transition) after zero field cooling; (3) a third image was acquired at 143 K after zero field warming. The same observation was carried out in the second tilt direction, i.e., using a tilt angle of -30°. Each experiment was repeated to assess the reproducibility. The Lorentz images, which are shown in Figure 10, were always acquired at remanence. Electron holograms were also acquired to determine the local magnetic field directions. The viewing direction was close to $[110]_c$.

The remanent magnetic states that were recorded initially at 143 K have large magnetic domains separated by 90° or 180° domain walls (Figure 10a, d, g and j). The configurations of the magnetic domains are identical in the first and second experiments, implying that the magnetic domain walls form in positions that are energetically favorable, as dictated by the local demagnetizing fields, the geometry of the specimen edge, the uneven specimen thickness and defects such as grain boundaries.

At 103 K after zero field cooling, the magnetic domains become smaller and are mostly separated by 180° domain walls, except for close to the specimen edge (Figure 10b, e, h and k). There are also needle-like magnetic domains present, where the magnetization directions deviate lightly from that in the parent domain. On the whole, however, there is a good correspondence between magnetization directions observed above and below the Verwey transition. In the center of the images, for example, the magnetization follows the specimen edge in the cubic phase, and both the direction and the sense of this magnetization are preserved at the specimen edge in the monoclinic phase. Similar preservation of magnetization directions can be seen in the upper left corner of the images, where the choice of easy axis direction and the formation of 180° magnetic domain walls in the monoclinic phase closely match the magnetization pattern observed in the cubic phase. These observations provide direct evidence that at least part of the overall pattern of magnetization in the cubic phase is preserved in the monoclinic phase during zero field cooling. The local differences in magnetization direction between the initial cubic and the monoclinic phase and between the first and second experiments could be related to differences in the positions where crystallographic monoclinic domains nucleate, to differences in the propagation speeds of the monoclinic domains and to magnetic interactions with neighboring domains.

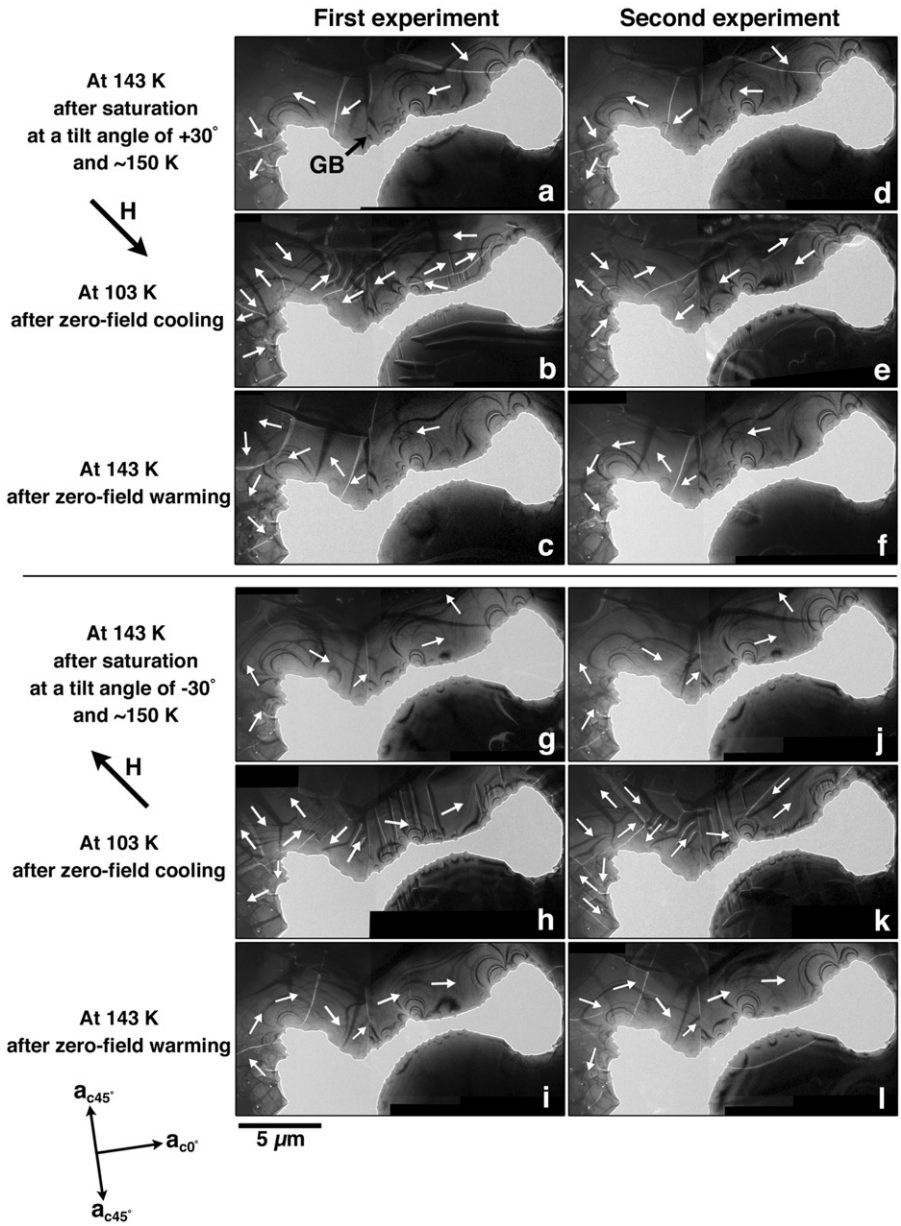

Figure 10. Lorentz images acquired during cycles of zero field cooling and warming through the Verwey transition. The experiment was repeated twice (first and second experiments) for each of two different applied field directions (a–f and g–l). The arrows marked 'H' indicate the applied magnetic field directions. The small white arrows show local magnetization directions inferred by the comparison of Lorentz images and electron holograms. The three arrows shown at the bottom indicate the projected cubic axes of a grain located in the center of the image; the symbols '$a_{c0°}$' and '$a_{c45°}$' refer to principal cubic axes that are oriented in-plane and at 45° to the plane of the specimen, respectively. The Lorentz images were acquired at an underfocus of 1.3 mm. GB: grain boundary.

In the remanent magnetic states that were recorded at 143 K after zero field warming, dense magnetic domain walls disappear and large magnetic domains develop (Figure 10c, f, i and l). Despite some differences in the positions of specific domain walls, the overall pattern of magnetization directions in the initial cubic phase and the cubic phase formed after warming through the Verwey transition correspond roughly to one another. A similar behavior is observed in each experiment, suggesting that the zero field warming states are restored approximately to their initial states, preserving the direction of remanence imparted before cooling. Magnetic fields created at the nucleation sites of cubic domains propagate to other regions which have not yet transformed and influence the overall magnetic microstructure in the cubic phase after zero field warming. As before, small differences between the magnetic structures in the first and second experiments may be related to differences in the magnetic structures seen below the transition, the position where the transition to the cubic phase take place first during warming and different propagation speeds of the transforming cubic domains (see Supplementary Movie 1).

Özdemir et al. [17] reported a value for the saturation remanence of magnetite after zero field cooling from 300 to 5 K and then zero field warming back to 300 K that was 55% of the original saturation remanence measured at 300 K for a sample with a 220 nm grain size, which is close to that in our specimen geometry (the TEM specimen thickness is ~200 nm). In other words, the magnetization (≈magnetic structure) that remained after zero field warming is similar to that measured initially at 300 K (at least the same magnetic sign), but is not exactly the same. These aspects can be seen qualitatively in the observations described above. We have also seen a reorganization of magnetic domains and ferroelastic twins below the transition (Figure 4), which may partly explain the small continuous increase in saturation remanence below the transition reported by Özdemir et al. [17]. However, it is difficult to discuss this point without more extensive experimental measurements.

3.9. *Magnetic domain rearrangement at the isotropic point*

The relationship between the magnetic transition at the isotropic point and the Verwey transition has been discussed for a long time [18]. Although many studies have argued that there are two different low temperature transitions (e.g., [48]), King et al. [49] suggested that they are a single transition. At the isotropic point, at ~130 K, the magnetic easy axis changes from $\langle 100 \rangle_c$ to $\langle 111 \rangle_c$ on warming. Consequently, some rearrangement of magnetic domains is expected.

Figure 11 shows video frames, which were recorded through the Verwey transition during zero field warming (Supplementary Movie 1). Figure 11(a) shows a characteristic magnetic structure, which was recorded just below the Verwey transition. At 120 K, dramatic changes in magnetic and strain (diffraction) contrast occur, lasting for 10–20 s during a temperature ramp of 0.07°C/s. After these dramatic changes, the local magnetic structure is modified further slightly, perhaps as a result of local strains and/or magnetic fields (Figure 11b). This modification ends at a temperature of a few degrees above the Verwey transition temperature (Figure 11c). Above 122 K, there are no noticeable changes in either magnetic or diffraction contrast (Figure 11d), providing no conclusive evidence for a change in easy axis direction.

The fact that microscopy observations are generally limited in their field of view may account for the fact that we have not seen a magnetic rearrangement through the isotropic point during zero field cooling or warming. The thin specimen shape with an irregular

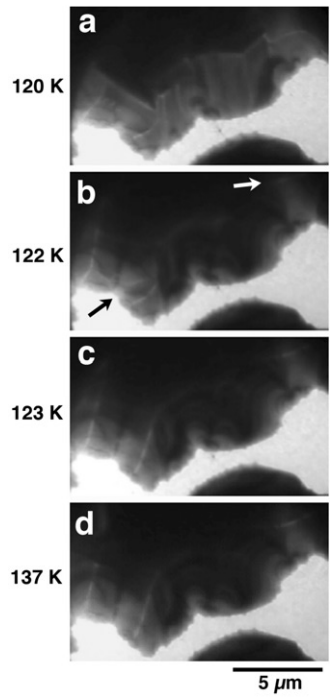

Figure 11. Selected frames from a video recording of Lorentz images acquired while warming the magnetite specimen through the Verwey and isotropic transitions in zero field. (a, b) Dramatic changes in magnetic and strain contrast start after a few seconds at 120 K and last for 10–20 s. (b, c) Small modifications to domain walls occur at 122–123 K. The white arrow in (b) shows a magnetic domain wall that moved in (c) and the black arrow shows a magnetic domain wall that disappeared in (c). (d) Lorentz image recorded at 137 K, showing no significant difference from (c).

specimen edge may also be responsible, as some magnetic domain walls appear to be pinned at the specimen edge (Figure 11c). Magnetoelastic anisotropy may also be more important in this temperature range rather than magnetocrystalline anisotropy [22], and when the sample passes through the Verwey transition during warming, strain fields associated with crystal defects may immediately capture magnetic domain walls, which were released from pinning sites (e.g., ferroelastic twin walls) in the monoclinic phase. Saturation remanence measurements made during zero field warming show remanent magnetizations that are almost constant above the Verwey transition [17,22], which is consistent with our observations.

4. Conclusion

We have studied the crystallographic and magnetic properties of synthetic magnetite above and below the Verwey transition using TEM. The crystal symmetry of the low temperature phase was confirmed to be monoclinic *Cc*. The local crystal orientation and the *c*-axis direction of the monoclinic phase can be determined by means of electron diffraction, albeit with some limitations. The low temperature monoclinic phase has closely spaced magnetic domains separated by 90° or 180° magnetic domain walls, which are defined

strictly by underlying monoclinic ferroelastic twin domains with an $[001]_m$ easy axis resulting from large magnetocrystalline anisotropy. Below the Verwey transition, strong interactions are observed between magnetic domain walls and twin domain walls. The most striking feature is that magnetic domain walls are strongly pinned by Type 1 and Type 1′ twin boundaries and return to their positions reproducibly after the application of large magnetic fields (up to ~2 T), since these twin boundaries cannot easily be displaced by magnetic fields. Furthermore, magnetic domains in magnetite above or below the Verwey transition can inherit a part of their magnetization from the prior phase during zero field cooling or zero field warming through the Verwey transition. Our results can be useful for interpreting low temperature magnetic properties of magnetite measured using bulk methods, which are widely used in rock magnetism and paleomagnetism and may provide new insights for understanding ferromagnetic and ferroelastic interactions as seen in many multiferroic materials.

Supplementary movie

Supplementary Movie 1. Lorentz image acquired while warming the magnetite specimen through the Verwey transition in zero field, showing nucleation and growth of the cubic phase within the monoclinic phase. Magnetic fields generated in regions where cubic domains nucleate propagate to other regions that have not been transformed to the cubic phase yet. No noticeable changes are observed above 122 K in either magnetic or strain contrast, while small modifications to magnetic domains occur after dramatic changes at the Verwey transition. The field of view is 18 μm.

Acknowledgements

We thank Y. Matsui, T. Yokosawa and J.M. Zuo for valuable discussions. This work was supported by the European Science Foundation (ESF) under the EUROCORES program EuroMinScI, through contract number ERAS-CT-2003-980409 of the European Commission, DG Research, FP6, and through NERC Grant NE/D002036/1.

References

[1] E.J.W. Verwey, *Electronic conduction of magnetite (Fe_3O_4) and its transition point at low temperature*, Nature 144 (1939), pp. 327–328.
[2] F. Walz, *The Verwey transition – A topical review*, J. Phys. Cond. Matter. 14 (2002), pp. R285–R340.
[3] K. Kato, S. Iida, K. Yanai, and K. Mizushima, *Ferrimagnetic ferroelectricity of Fe_3O_4*, J. Magn. Magn. Mater. 31–34 (1983), pp. 783–784.
[4] M. Tanaka, *Convergent-beam characterization of some oxides which undergo structural phase transitions*, in *Proceedings of the 45th Annual Meeting of the Electron Microscopy Society of America*, G.W. Bailey, ed., San Francisco Press, USA, 1987, pp. 20–23.
[5] J. Yoshida and S. Iida, *X-ray diffraction study on the low temperature phase of magnetite*, J. Phys. Soc. Jpn. 42 (1977), pp. 230–237.
[6] M. Iizumi, T.F. Kötzle, G. Shirane, S. Chikazumi, M. Matsui, and S. Todo, *Structure of magnetite (Fe_3O_4) below the Verwey transition temperature*, Acta Cryst. B38 (1982), pp. 2121–2133.
[7] J.M. Zuo, J.C.H. Spence, and W. Petuskey, *Charge ordering in magnetite at low temperatures*, Phys. Rev. B 42 (1990), pp. 8451–8464.

[8] J.P. Wright, J.P. Attfield, and P.G. Radaelli, *Charge ordered structure of magnetite Fe_3O_4 below the Verwey transition*, Phys. Rev. B 66 (2002), p. 214422.
[9] G.T. Rado and J.M. Ferrari, *Electric field dependence of the magnetic anisotropy energy in magnetite (Fe_3O_4)*, Phys. Rev. B 12 (1975), pp. 5166–5174.
[10] K. Kato and S. Iida, *Magnetoelectric effects of Fe_3O_4 at 4.2 K*, J. Phys. Soc. Jpn 50 (1981), pp. 2844–2850.
[11] K. Shiratori, E. Kita, G. Kaji, A. Tasaki, S. Kimura, I. Shindo, and K. Kohn, *Magnetoelectric effect of Fe_3O_4 at 77 K. I. Crystal symmetry*, J. Phys. Soc. Jpn 47 (1979), pp. 1779–1787.
[12] Y. Miyamoto, M. Kobayashi, and S. Chikazumi, *Anomaly of pyroelectricity in magnetite below 10 K*, J. Phys. Soc. Jpn 55 (1986), pp. 660–665.
[13] C. Medrano, M. Schlenker, J. Baruchel, J. Espeso, and Y. Miyamoto, *Domains in the low-temperature phase of magnetite from synchrotron-radiation X-ray topographs*, Phys. Rev. B 59 (1999), pp. 1185–1195.
[14] K. Abe, Y. Miyamoto, and S. Chikazumi, *Magnetocrystalline anisotropy of low temperature phase of magnetite*, J. Phys. Soc. Jpn 41 (1976), pp. 1894–1902.
[15] L.R. Bickford, J.M. Brownlow, and R.F. Penoyer, *Magnetocrystalline anisotropy in cobalt-substituted magnetic single crystals*, Proc. I.E.E. B104 (1957), pp. 238–244.
[16] B.M. Moskowitz, M. Jackson, and C. Kissel, *Low-temperature magnetic behavior of titanomagnetites*, Earth Planet. Sci. Lett. 157 (1998), pp. 141–149.
[17] Ö. Özdemir, D.J. Dunlop, and B.M. Moskowitz, *Changes in remanence, coercivity and domain state at low temperature in magnetite*, Earth Planet. Sci. Lett. 194 (2002), pp. 343–358.
[18] A.R. Muxworthy and E. McClelland, *Review of the low-temperature magnetic properties of magnetite from a rock magnetic perspective*, Geophys. J. Int. 140 (2000), pp. 101–114.
[19] A.V. Smirnov and J.A. Tarduno, *Magnetic field control of the low temperature magnetic properties of stoichiometric and cation-deficient magnetite*, Earth Planet. Sci. Lett. 194 (2002), pp. 359–368.
[20] A.V. Smirnov, *Memory of the magnetic field applied during cooling in the low-temperature phase of magnetite: Grain size dependence*, J. Geophys. Res. 111 (2006), p. B12S04.
[21] A. Kosterov, *Magnetic hysteresis of pseudo-single-domain and multidomain magnetite below the Verwey transition*, Earth Planet. Sci. Lett. 186 (2001), pp. 245–253.
[22] Ö. Özdemir and D.J. Dunlop, *Low-temperature properties of a single crystal of magnetite oriented along principal magnetic axes*, Earth Planet. Sci. Lett. 165 (1999), pp. 229–239.
[23] A. Kosterov and K. Fabian, *Twinning control of magnetic properties of multidomain magnetite below the Verwey transition revealed by measurements on individual particles*, Geophys. J. Int. 174 (2008), pp. 93–106.
[24] B. Carter-Stiglitz, B. Moskowiz, P. Solheid, T.S. Berquó, M. Jackson, and A. Kosterov, *Low-temperature magnetite behavior of multidomain titanomagnetites: TM0, TM16, and TM35*, J. Geophys. Res. 111 (2006), p. B12S05.
[25] S. Chikazumi, K. Chiba, K. Suzuki, and T. Yamada, *Electron microscopic observation of low temperature phase of magnetite*, in *Ferrites: Proceedings of the International Conference*, Y. Hoshino, S. Iida, and S. Sugimoto, eds., University of Tokyo Press, Japan, 1971, pp. 595–597.
[26] T. Yamada, K. Suzuki, and S. Chikazumi, *Electron microscopy of orthorhombic phase in magnetite*, Appl. Phys. Lett. 13 (1968), pp. 172–174.
[27] N. Otsuka and H. Sato, *Observation of the Verwey transition in Fe_3O_4 by high-resolution electron-microscopy*, J. Solid State Chem. 61 (1986), pp. 212–222.
[28] K. Moloni, B.M. Moskowitz, and E.D. Dahlberg, *Domain structures in single crystal magnetite below the Verwey transition as observed with a low-temperature magnetic force microscope*, Geophys. Res. Lett. 23 (1996), pp. 2851–2854.
[29] T. Kasama, N.S. Church, J.M. Feinberg, R.E. Dunin-Borkowski, and R.J. Harrison, *Direct observation of ferromagnetic/ferroelastic domain interactions in magnetite below the Verwey transition*, Earth Planet. Sci. Lett. 297 (2010), pp. 10–17.
[30] T. Kasama, R.E. Dunin-Borkowski, T. Asaka, R.J. Harrison, R.K.K. Chong, S.A. McEnroe, E.T. Simpson, Y. Matsui, and A. Putnis, *The application of Lorentz transmission electron*

microscopy to the study of lamellar magnetism in hematite-ilmenite, Am. Mineral. 94 (2009), pp. 262–269.
[31] R.J. Harrison, R.E. Dunin-Borkowski, and A. Putnis, *Direct imaging of nanoscale magnetic interactions in minerals*, Proc. Nat. Acad. Sci. 99 (2002), pp. 16556–16561.
[32] T. Kasama, P. Barpanda, R.E. Dunin-Borkowski, S.B. Newcomb, M.R. McCartney, F.J. Castaño, and C.A. Ross, *Off-axis electron holography of individual pseudo-spin-valve thin film magnetic elements*, J. Appl. Phys. 98 (2005), p. 013903.
[33] T. Kasama, R.E. Dunin-Borkowski, and W. Eerenstein, *Off-axis electron holography observation of magnetic microstructure in a magnetite (001) thin film containing antiphase domains*, Phys. Rev. B 73 (2006), p. 104432.
[34] T. Kasama, M. Pósfai, R.K.K. Chong, A.P. Finlayson, P.R. Buseck, R.B. Frankel, and R.E. Dunin-Borkowski, *Magnetic properties, microstructure, composition and morphology of greigite nanocrystals in magnetotactic bacteria from electron holography and tomography*, Am. Mineral. 91 (2006), pp. 1216–1229.
[35] T. Kasama, R.E. Dunin-Borkowski, M.R. Scheinfein, S.L. Tripp, J. Liu, and A. Wei, *Reversal of flux closure states in cobalt nanoparticle rings with coaxial magnetic pulse*, Adv. Mater. 20 (2008), pp. 4248–4252.
[36] T. Kasama, R.E. Dunin-Borkowski, and M. Beleggia, *Electron holography of magnetic materials*, in *Holography – Different Fields of Application*, F.A. Monroy Ramírez, ed., InTech, 2011, pp. 53–80.
[37] P.A. Stadelmann, *JEMS – EMS java version*. http://cimewww.epfl.ch/people/stadelmann/jemsWebSite/jems.html.
[38] R.J. Harrison, S.A.T. Redfern, and E.K.H. Salje, *Dynamical excitation and anelastic relaxation of ferroelastic domain walls in $LaAlO_3$*, Phys. Rev. B: Condens. Matter 69 (2004), p. 144101.
[39] R.J. Harrison and E.K.H. Salje, *The noise of the needle: Avalanches of a single progressing needle domain in $LaAlO_3$*, Appl. Phys. Lett. 97 (2010), p. 021907.
[40] R.J. Harrison and E.K.H. Salje, *Ferroic switching, avalanches and the Larkin length: Needle domains in $LaAlO_3$*, Appl. Phys. Lett. 99 (2011), p. 151915.
[41] J. Yoshida and S. Iida, *X-ray study of the phase transition in magnetite*, J. Phys. Soc. Jpn 47 (1979), pp. 1627–1633.
[42] Ö. Özdemir, S. Xu, and D.J. Dunlop, *Closure domains in magnetite*, J. Geophys. Res. 100 (1995), pp. 2193–2209.
[43] A.R. Muxworthy and W. Williams, *Micromagnetic models of pseudo-single domain grains of magnetite near the Verwey transition*, J. Geophys. Res. 140 (1999), pp. 29203–29217.
[44] J.F.J Bryson, T. Kasama, R.E. Dunin-Borkowski, and R.J. Harrison, *Ferrimagnetic/ferroelastic domain interactions in magnetite below the Verwey transition. Part II: Micromagnetic and image simulations*, Phase Trans., this issue.
[45] M. Beleggia and Y. Zhu, *Electron-optical phase shift of magnetic nanoparticles: I. Basic concepts*, Philos. Mag. 83 (2003), pp. 1045–1057.
[46] D. Watanabe, T. Sekiguchi, T. Tanaka, T. Wakiyama, and M. Takahashi, *Study of the temperature dependence of the magnetization direction in cobalt single crystals by 1 MV Lorentz electron microscopy*, Jpn J. Appl. Phys. 21 (1982), pp. L179–L181.
[47] C.H. Li, *Magnetic properties of magnetite crystals at low temperature*, Phys. Rev. 40 (1932), pp. 1002–1012.
[48] R. Aragón, D.J. Buttery, J.P. Shepherd, and J.M. Honig, *Influence of non-stoichiometry on the Verwey transition*, Phys. Rev. B 31 (1985), pp. 430–436.
[49] J.G. King, W. Williams, C.D.W. Wilkinson, S. McVitie, and J.N. Chapman, *Magnetic properties of arrays produced by the method of electron beam lithography*, Geophys. Res. Lett. 23 (1996), pp. 2847–2850.